Journal of Applied Electrochemistry (2020) 50:93–109
https://doi.org/10.1007/s10800-019-01372-5

RESEARCH ARTICLE

Analysis on discharge behavior and performance of As- and B-doped silicon anodes in non-aqueous Si–air batteries under pulsed discharge operation

Yasin Emre Durmus[1] · Christoph Roitzheim[1] · Hermann Tempel[1] · Florian Hausen[1,2] · Yair Ein-Eli[3] · Hans Kungl[1] · Rüdiger-A. Eichel[1,2]

Received: 16 July 2019 / Accepted: 14 November 2019 / Published online: 2 December 2019

Abstract

Very high theoretical specific energies and abundant resource availability have emerged interest in primary Si–air batteries during the last decade. When operated with highly doped Si anodes and $EMIm(HF)_{2.3}F$ ionic liquid electrolyte, specific energies up to 1660 Wh kg_{Si}^{-1} can be realized. Owing to their high-discharge voltage, the most investigated anode materials are ⟨100⟩ oriented highly As-doped Si wafers. As there is substantial OCV corrosion for these anodes, the most favorable mode of operation is continuous discharge. The objective of the present work is, therefore, to investigate the discharge behavior of cells with ⟨100⟩ As-doped Si anodes and to compare their performance to cells with ⟨100⟩ B-doped Si anodes under pulsed discharge conditions with current densities of 0.1 and 0.3 mA cm^{-2}. Nine cells for both anode materials were operated for 200 h each, whereby current pulse time related to total operating time ranging from zero (OCV) to one (continuous discharge), are considered. The corrosion and discharge behavior of the cells were analyzed and anode surface morphologies after discharge were characterized. The performance is evaluated in terms of specific energy, specific capacity, and anode mass conversion efficiency. While for high-current pulse time fractions, the specific energies are higher for cells with As-doped Si anodes, along with low-current pulse fractions the cells with B-doped Si anodes are more favorable. It is demonstrated, that calculations for the specific energy under pulsed discharge conditions based on only two measurements—the OCV and the continuous discharge—match very well with the experimental data.

Electronic supplementary material The online version of this article (https://doi.org/10.1007/s10800-019-01372-5) contains supplementary material, which is available to authorized users.

✉ Yasin Emre Durmus
y.durmus@fz-juelich.de

[1] Fundamental Electrochemistry (IEK-9), Institute of Energy and Climate Research, Forschungszentrum Jülich GmbH, 52425 Jülich, Germany

[2] Institute of Physical Chemistry, RWTH Aachen University, 52074 Aachen, Germany

[3] Department of Materials Science and Engineering, Technion-Israel Institute of Technology, 3200003 Haifa, Israel

Graphic abstract

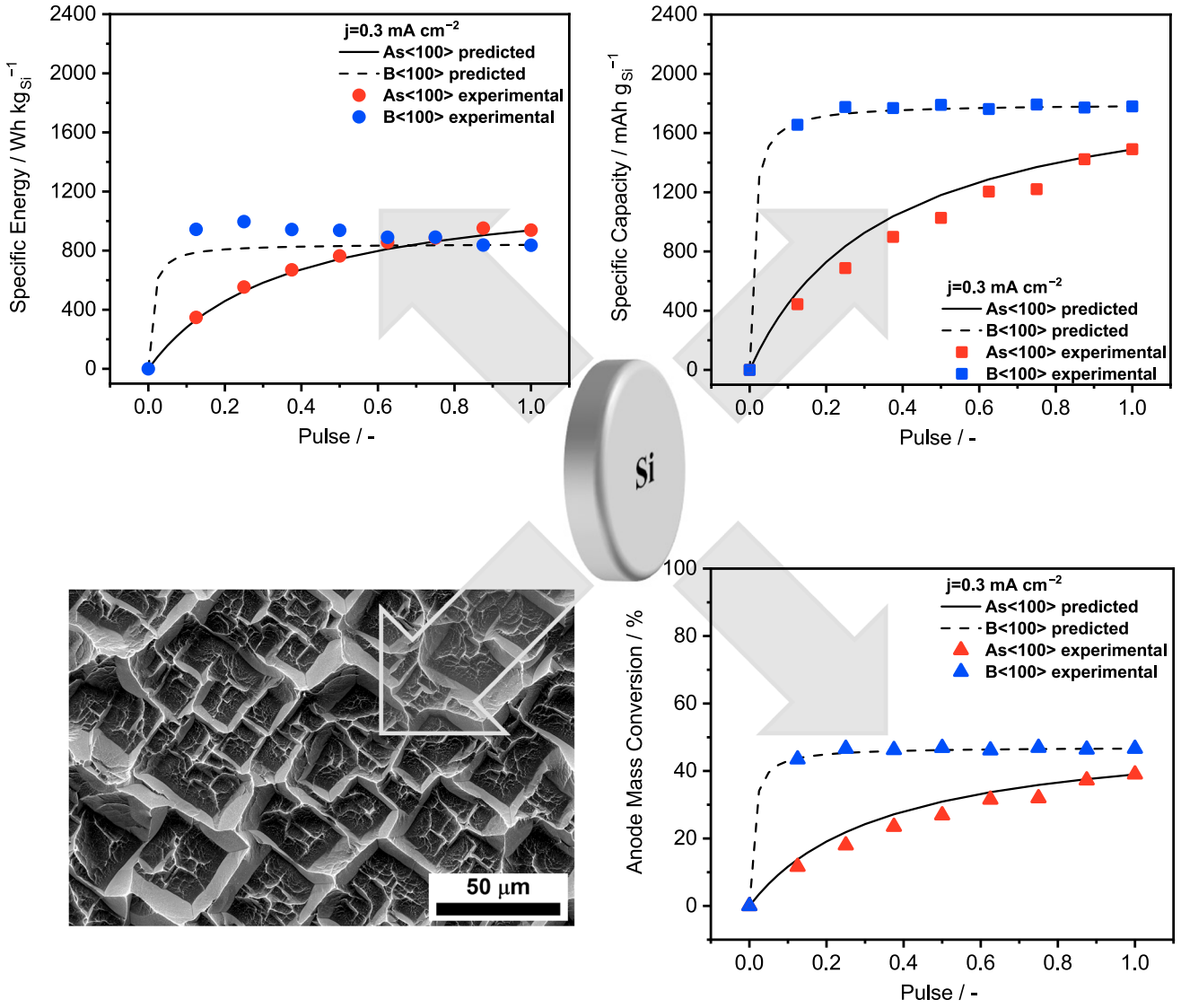

Keywords Battery · Si–air · Non-aqueous · Pulsed discharge · Corrosion

1 Introduction

Increased demand on new battery technologies for electrical energy storage devices, possessing very high-theoretical energy densities and being abundant in terms of resource availability motivate the ongoing research on metal–air batteries progressively [1–9]. Among the resource-efficient anode materials, the highest theoretical energy densities can be realized with aluminium and silicon; specific energies are 8091 Wh kg_{Al}^{-1} and 8461 Wh kg_{Si}^{-1} while energy densities are 21,845 Wh L_{Al}^{-1} and 19,715 Wh L_{Si}^{-1}. Considering the resource efficiency, aluminium and silicon are also most favorable with respect to their crustal abundance, which amounts to $10^{4.9}$ and $10^{5.5}$ ppm [10] and to their availability, as indicated by the annual production. The world production of aluminium and silicon were 57,600 and 7200 metric tons in 2016, respectively [11]. In addition to high-specific energy and resource effectiveness, future energy scenarios based on fluctuating renewable energy supply require storage devices to be capable of being operated under dynamic conditions [12].

Long run continuous discharge of primary Si–air batteries has already been demonstrated along with non-aqueous $EMIm(HF)_{2.3}F$ ionic liquid electrolyte in cells with static electrolyte supply [13] and in cells refilled by a pumping system using aqueous KOH electrolyte [14]. Regarding the

performance point of view, it is advantageous to use the ionic liquid electrolyte which provides current densities one order of magnitude higher with corrosion being one order of magnitude lower than for the cells operated with KOH. In spite of the lower performance, cost effectiveness of the KOH electrolyte makes this system competitive to the non-aqueous Si–air system. Moreover, the aqueous Si–air batteries are in a very early stage of development, so there is still a wide scope of improvements for this system [14–17].

Due to possessing properties such as high conductivity, low viscosity, wide electrochemical window, stability in air [18–20], and in particular the capability to dissolve native oxide films from surfaces (e.g. silicon [21] and aluminium [22]), $EMIm(HF)_{2.3}F$ electrolyte is favorable for application in metal–air batteries. The development of Si–air batteries with $EMIm(HF)_{2.3}F$ electrolyte started in 2009, when the proof of concept was established [23] and, subsequently, the discharge capacities up to 26.7 mAh from a cell with 0.5 cm^2 anode surface area were corroborated [13]. Since then, focus of the further research was on electrochemical mechanisms, on factors influencing the end of discharge [24, 25], and—with respect to material selection—on performance investigations depending on silicon anode type [26]. In general, pore clogging by silicon oxide deposits at the cathode side [13, 25] and enhanced resistivity at the anode interface [24] were identified as factors contributing to the discharge limitations. However, the mechanisms that lead to the discharge termination are still under discussion.

Considering the chemical characteristics of the ionic liquid, the $EMIm(HF)_{2.3}F$ electrolyte contains two types of anions $(HF)_2F^-$ and $(HF)_3F^-$, which play a crucial role in the electrochemical mechanisms according to the following reactions [13]:

$$\text{Anodic: } Si + 12(HF)_2F^- \rightleftarrows SiF_4 + 8(HF)_3F^- + 4e^-, \quad (1)$$

$$\text{Cathodic: } O_2 + 12(HF)_3F^- + 4e^- \rightleftarrows 2H_2O + 16(HF)_2F^-, \quad (2)$$

$$SiF_4 + 2H_2O + 4(HF)_2F^- \rightleftarrows SiO_2 + 4(HF)_3F^-, \quad (3)$$

where SiF_4 is a gaseous specie which reacts with water and di-hydrogenated fluoride anions at the cathode side to produce the end product, silicon dioxide.

Until now, Si anodes employed in the Si–air batteries were highly doped single-crystalline Si wafers. The nature of Si as being a semiconductor makes doping an essential process to improve the electronic conductivities of Si electrodes. Investigations of the dopant types have already been provided by potentiodynamic polarization experiments [13, 23, 26] and galvanostatic discharge experiments [26]. According to the potentiodynamic polarization experiments, the OCP and the anodic potentials are substantially higher for As- than for B-doped Si wafer anodes. These trends were confirmed by further investigations in the intermediate term discharge behavior; however, the analysis of mass losses in these experiments revealed substantially lower corrosion rates for the B-doped Si anodes [26]. Nevertheless, the specific energies under continuous discharge were higher for the ⟨100⟩ As-doped Si anodes, because their higher cell voltages overcompensated the effects from corrosion mass losses [26].

Since corrosion is a parasitic process that is also present under OCV, intermittent discharge would influence the specific energies for both anode materials. The quantitative effects on the specific energies w_s depend on discharge voltages E_{dis}, discharge capacities Q_s, mass changes from discharge Δm_{dis}, corrosion under discharge $\Delta m_{corr,dis}$ and OCV $\Delta m_{corr,OCV}$. With OCV corrosion being more severe in ⟨100⟩ As-doped Si compared to ⟨100⟩ B-doped Si anodes, the utilized specific energies for the latter would be higher under intermittent discharge conditions. Therefore, an investigation on operating conditions which might provide higher specific energies for the ⟨100⟩ B-doped Si anodes over the ⟨100⟩ As-doped Si anodes is addressed.

Specifically, in the present work, the intermittent discharge behavior of Si–air cells with ⟨100⟩ oriented As- and B-doped Si anodes is analyzed based on experiments with current densities of 0.1 and 0.3 mA cm^{-2} over 200 h operation time. For each material and current density, the current pulse time related to the total operation time is varied in nine experiments which are evaluated with respect to time-dependent cell voltage profiles, corrosion and specific energy. To understand the behavior of individual electrodes, additional discharge experiments are studied in half-cells and compared to corresponding full-cells. The corrosion behavior under different pulse conditions is reported in terms of corrosion masses and corrosion rates. Moreover, the morphologies of the anode surfaces after discharge are characterized by scanning electron microscopy (SEM). It is demonstrated, that the specific energies under pulsed discharge can be predicted based on calculations that use the data sets from an OCV and a continuous discharge experiment.

2 Experimental

2.1 Materials preparation

Highly As- and B-doped single-crystalline silicon wafers (University Wafer, USA) with specifications as listed in Table 1, were cut into 12 × 12 mm sized squared pieces to be used as anodes. Before the electrochemical measurements, the anode surfaces were treated with plasma (PICO, Diener). A two-step plasma treatment was applied to Si wafers to volatilize organic contaminations and to remove the native oxide layer on the silicon surfaces. First, a treatment with

Table 1 The physical properties of Si wafers used in this study

Type	Dopant	Orientation	Thickness (μm)	Resistivity (Ω cm)	Doping concentration[a] (cm^{-3})
n	As	⟨100⟩	625	0.001–0.007	9.0×10^{19}–0.74×10^{19}
p	B	⟨100⟩	525	0.001–0.005	1.26×10^{20}–2.05×10^{19}

[a]Doping concentrations are obtained by the calculator from the website of the provider (University Wafer)

oxygen/argon plasma (60% O_2/40% Ar) was employed, which was followed by an argon/sulfur hexafluoride plasma (50% SF_6/46% Ar/4% O_2). A room temperature ionic liquid $EMIm(HF)_{2.3}F$ from Morita Chemical Industries, Japan was used as an electrolyte without further treatment. Commercial air-electrodes (E4b type, Electric Fuel Ltd., Israel) consisting of a stainless-steel mesh embedded into carbon black with manganese dioxide catalyst were used for air cathodes. The air side of these cathodes is covered with a Teflon layer.

2.2 Electrochemical setups

Si–air full-cells for discharge experiments were assembled using a silicon wafer as anode, the ionic liquid $EMIm(HF)_{2.3}F$ as electrolyte and a porous carbon-based air-electrode as cathode. The cell setup made from poly(methyl methacrylate) was constructed following the design by Technion [13]. The setup provides a geometric surface area of 0.44 cm^2 for both anode and cathode electrodes with an electrolyte volume of 0.6 ml. A three electrode setup used for the half-cell experiments was assembled by the same components with a silicon wafer or an air-electrode as working electrode, a platinum wire as counter electrode, and a self-prepared $FeCp_2/FeCp_2^+$ gel-based reference electrode (see [27] for further details on reference electrode). All experiments were carried out in a climate chamber (Binder KMF115) at 25 °C and 50% relative humidity. The electrochemical measurements were controlled via a Bio-Logic VMP3 potentiostat and the experimental data were evaluated by the EC-lab software. The pulsed discharge experiments were set up for a total operating time of 200 h with current densities of 0.1 and 0.3 mA cm^{-2}. The operating conditions for different pulse durations were characterized by the current pulse time fraction $p = t_{dis}/(t_{dis} + t_{OCV})$, where t_{dis} and t_{OCV} correspond to total discharge and open-circuit voltage times during the experiments, respectively. OCV ($p = 0$), continuous discharge ($p = 1$), and the current pulse time fraction ($p = 0.125, 0.25, 0.375, 0.5, 0.625, 0.75, 0.875$) experiments were carried out for each current density.

2.3 Corrosion rates

The corrosion rates of Si anodes were determined via the mass loss method. The silicon wafers were weighed before assembling the cell (m_i) using a micro balance with an accuracy of 0.01 mg (XA205, Mettler Toledo). After the experiments, the cells were directly disassembled, the silicon wafers were rinsed with deionized water, dried, and weighed again (m_f) to obtain the total mass loss during the discharge runs. The total mass loss ($\Delta m_{tot} = m_i - m_f$) was afterwards used to calculate the mass loss due to corrosion (Δm_{corr}) by $\Delta m_{corr} = \Delta m_{tot} - \Delta m_{dis} = \Delta m_{tot} - ((I_{dis} \cdot t_{dis})/(n \cdot F/M_{Si}))$ where n is the number of charge carriers ($4e^-$), F is the Faraday constant and M_{Si} is the molecular mass of silicon. The anode mass conversion efficiencies were obtained by $\Delta m_{dis}/\Delta m_{tot}$.

2.4 Surface characterizations

SEM was used to characterize the morphology of the surfaces of Si anodes after discharge experiments. The images were recorded with a Quanta 650 (FEI, USA). Applied acceleration voltage in the SEM imaging measurements was 5 kV.

3 Results and discussion

3.1 Time evolution of cell voltages under pulsed discharge

The intermittent discharge performance of Si–air cells under various current pulses with 0.1 and 0.3 mA cm^{-2} are shown in Figs. 1 and 2 for As ⟨100⟩ and B ⟨100⟩ Si anodes, respectively. In these figures, the voltage profiles for 200 h OCV ($p = 0$) and 200 h continuous discharge ($p = 1$) are also demonstrated. As a general trend, the time evolution of the cell voltages during intermittent discharge and OCV intervals follows the decay of the voltages for the continuous discharge and the continuous OCVs, respectively.

On switching between OCV and discharge during intermittent cell operation, there are only minor effects from polarization dynamics for cells with As-doped Si anodes. In contrast to that, following the switching off the current, cells with the B-doped Si anodes show pronounced overshooting of the voltages and subsequent relaxation effects back to voltages close to continuous OCV. This behavior does not induce any marked polarization dynamics on the cell voltages during the consecutive current pulse periods.

Considering the trends of the mean voltages during discharge and OCV periods under pulsed operation compared to those under 200 h continuous discharge or OCV, there are clear correlations related to the current pulse time

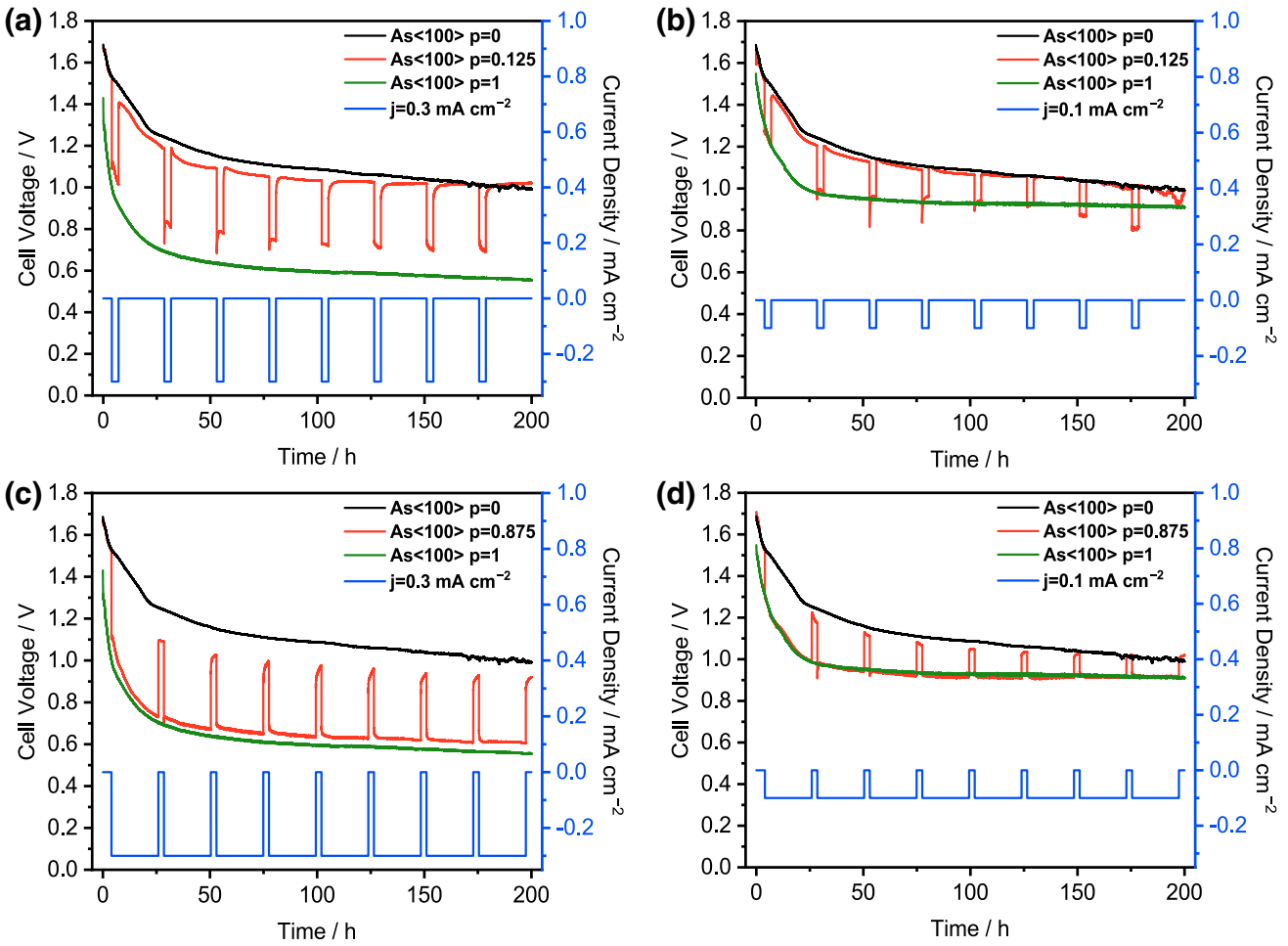

Fig. 1 Discharge profiles of the Si–air cells with ⟨100⟩ As-doped Si anodes during 200 h pulsed discharge under **a** current density of 0.3 mA cm^{-2} with current pulse time fraction $p=0.125$, **b** current density of 0.3 mA cm^{-2} with $p=0.875$, **c** current density of 0.1 mA cm^{-2} with $p=0.125$, and **d** current density of 0.1 mA cm^{-2} with $p=0.875$

fraction and the current densities for both cells with As- and B-doped Si anodes. In cells with As-doped Si anodes under low-current pulse time fractions, the mean voltages during their OCV periods are close to those for the 200 h OCV operation, whereas the mean voltages during the discharge periods are significantly higher than those under continuous discharge (Fig. 1a). In contrast to that, intermittent discharge with high-current pulse time fractions results in mean discharge voltages very close to those for the continuous discharge, while the mean voltages during the OCV periods are considerably lower than those for the 200 h OCV measurement (Fig. 1c). These features are more pronounced along with higher discharge currents (Fig. 1a, c vs. 1b, d). Similar behavior is also found for the cells with B-doped Si anodes considering the time profiles of the voltages after relaxation from the overshooting effects (Fig. 2a–d). The data for the time-averaged mean voltages during OCV and discharge periods depending on the current pulse time fraction are summarized in Fig. 3 for the cells with As- and B-doped Si anodes.

There is clearly a distinct influence of the dopant types on the electrochemical behavior of Si–air cells. Figure 3 demonstrates the comparison of the overall effects of the As- and B-dopants on the mean cell voltages over 200 h. The differences on the figure are solely related to dopant types as the cell setup (electrolyte, air cathode) was kept same in all experiments. Doping of Si electrodes with As yielded higher cell voltages under OCV and discharge in comparison to B-dopant. The large difference under OCV (≈ 400 mV) was lowered to 150 mV for continuous discharge experiments. Similar results have also been reported previously by potentiodynamic polarization experiments in half-cells [13, 26]. As confirmed by both, galvanostatic discharge and potentiodynamic polarization experiments, B-doped Si electrodes in $EMIm(HF)_{2.3}F$ electrolyte reveal more “passive-like” electrochemical behavior, which is reflected as lower cell voltages on the discharge profiles. The mechanisms underlying

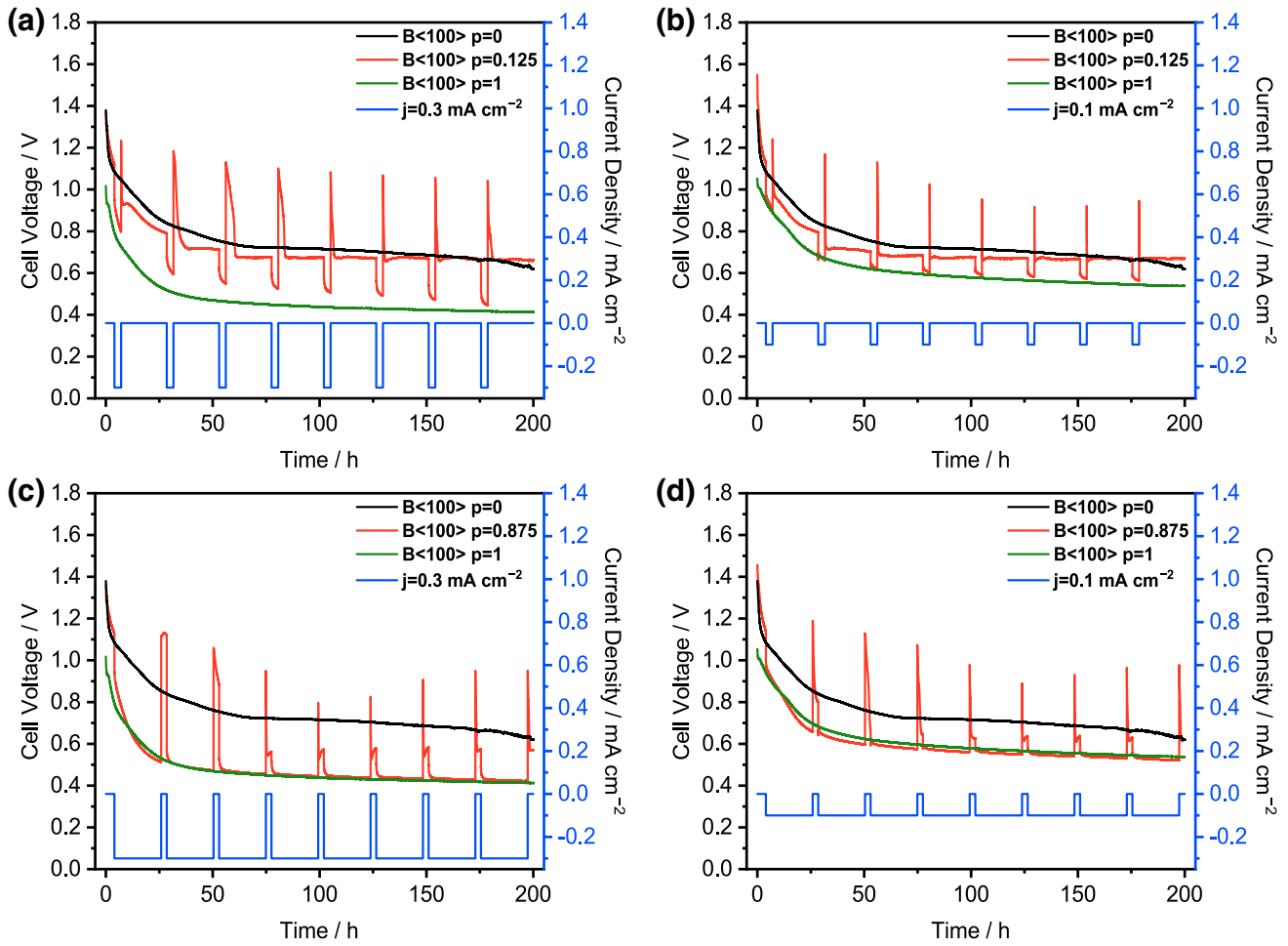

Fig. 2 Discharge profiles of the Si–air cells with ⟨100⟩ B-doped Si anodes during 200 h pulsed discharge under **a** current density of 0.3 mA cm^{-2} with current pulse time fraction $p=0.125$, **b** current density of 0.3 mA cm^{-2} with $p=0.875$, **c** current density of 0.1 mA cm^{-2} with $p=0.125$, and **d** current density of 0.1 mA cm^{-2} with $p=0.875$

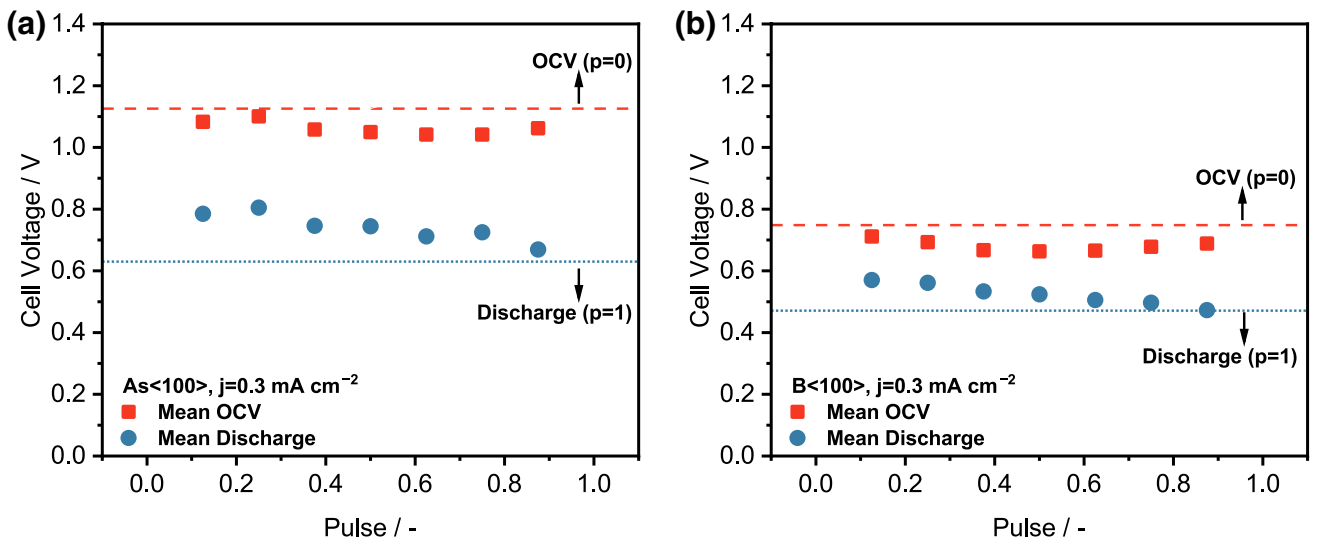

Fig. 3 Mean voltages of cells with As- and B-doped Si anodes during OCV and discharge periods under 0.3 mA cm^{-2} depending on pulse time fraction p. **a** As-doped Si anodes and **b** B-doped Si anodes

the passive-like behavior is, however, not well understood in the investigated ionic liquid.

The origin of the potential difference (at OCP) between As- and B-doped Si wafers can be understood by considering the energy band diagrams. Unlike for metals, the Fermi level of semiconductors lies between valence and conduction bands. Excluding the degenerated-case, position of the Fermi level within the energy band gap is determined by the concentration and type of dopant. In case of n-type Si (doped with Group V elements e.g. As), the Fermi level is located close to conduction band whereas it is close to valence band for p-type Si (doped with Group III elements e.g. B). The theoretical electrochemical potential of Si is defined by the Fermi level. Hence, for an ideal case in the same electrolyte, the difference between the Fermi levels of n-type Si and p-type Si results in variations on the open-circuit potentials. Detailed explanation on energy band diagrams can be found in [28–31].

3.2 Analysis of overshooting

To gain insights to the origin of the pronounced overshooting of the voltages during intermittent discharge profiles for cells with B-doped Si, half-cell experiments with B-doped Si, As-doped Si and carbon-based air cathode as the working electrodes are performed. Intermittent discharge experiments in half-cell setups are operated for 24 h under a discharge current density of 0.3 mA cm^{-2}. The half-cell potentials are measured versus the self-prepared Cp_2Fe/Cp_2Fe^+ gel-based reference electrode. For further investigations, full-cell experiments in two and three electrode configurations are also conducted under the same operating conditions.

In the half-cell with carbon-based air-electrode, the OCP drops from initially 0.3 V to 0.0 V approximately after 24 h intermittent operation (Fig. 4a, b). There is no significant decay of the potentials during the individual OCP steps; on the contrary the potentials gradually tend to equilibrate at higher values when switching to OCP. Also, the voltage drop of approximately 0.1 V on switching from actual OCP to discharge remains the same for each step. The time-dependent decay of the potentials occurs mainly during the individual discharge steps where the potentials decrease continuously. No overshooting effects when switching back from discharge to OCP are observed for this type of half-cell with carbon-based air-electrode.

The overall evolution of potentials for half-cells with As-doped Si electrodes shows a slight trend toward less negative OCP along with the operation time. In these cells, the OCP starts at − 1.4 V, increases during the initial OCP step in the positive direction to − 1.3 V and stabilizes around − 1.28 V after the 24 h intermittent discharge experiment (Fig. 4a). Subsequent to switching on the discharge current, the cell potential raises by 0.25 V after which the discharge potentials stabilize. On switching back from discharge to OCP there are no overshooting effects in half-cells with As-doped Si electrodes.

Quite different behavior is observed for the half-cells containing B-doped Si wafers regarding the overall development of the OCP during the operating time as well the overshooting behavior after switching to OCP (Fig. 4b). For the B-doped Si half-cell the OCP starts at − 1.1 V and increases in the positive direction to − 0.9 V during the first step. When initiating the discharge after this first OCP period, the potential rises by 0.15 V and remains constant at − 0.74 V during the discharge. Along with switching back to OCP after the discharge, a large potential drop of around 0.6 V in the negative direction is observed. The OCP shows only slight relaxation and stabilizes at − 1.3 V; thus, being almost 0.4 V more negative than right before the first discharge. The initial and subsequent discharge steps seem to activate processes that lead to more negative OCP in the following periods. However, the effects of this activation are limited to OCP since the potentials remain at the same level during all the discharge steps. In contrast to that, the OCP becomes slightly more negative in the following periods.

To compare the discharge profiles of the half-cells to those of the corresponding full-cell experiments, the results from half-cells with Si and carbon-based air electrodes are combined by subtracting the anodic potentials (Si electrodes) from the cathodic potential (air-electrode). The time profiles of the voltages for As-doped Si–air full-cells in a two-electrodes setup and those calculated from the half-cell experiments (Fig. 4c) are qualitatively very similar. Quantitatively, differences of 50 mV during the discharge and OCV periods are observed. In contrast to that, for the B-doped Si electrode, the behavior of the experimental voltages for full-cells vs. those calculated from half-cell show marked qualitative differences (Fig. 4d). Although in both types of cells the application of a discharge current pulse leads to a pronounced increase in subsequent OCV period, there are substantial differences with respect to the time behavior of the changes in OCV. While for the full-cell the enhanced OCV is only temporary, decaying to the previous value after approximately 2 h at the end of the intermittent OCV periods; in the half-cells, the higher level for the OCV is maintained permanently. Consequently, in voltage profiles for the full-cell experiments, the enhanced OCV after the discharge steps appears as an overshooting whereas in those of the half-cell experiment, the OCV remains almost constant at higher levels in comparison to initial OCV.

The analysis of the half-cells indicates that enhanced OCP and overshooting after discharge periods requires the presence of B-doped Si electrodes because overshooting of OCP is not observed in half-cells with As-doped Si electrode or air electrode. Moreover, the comparison with full-cell experiments leads to the conclusion that the effects

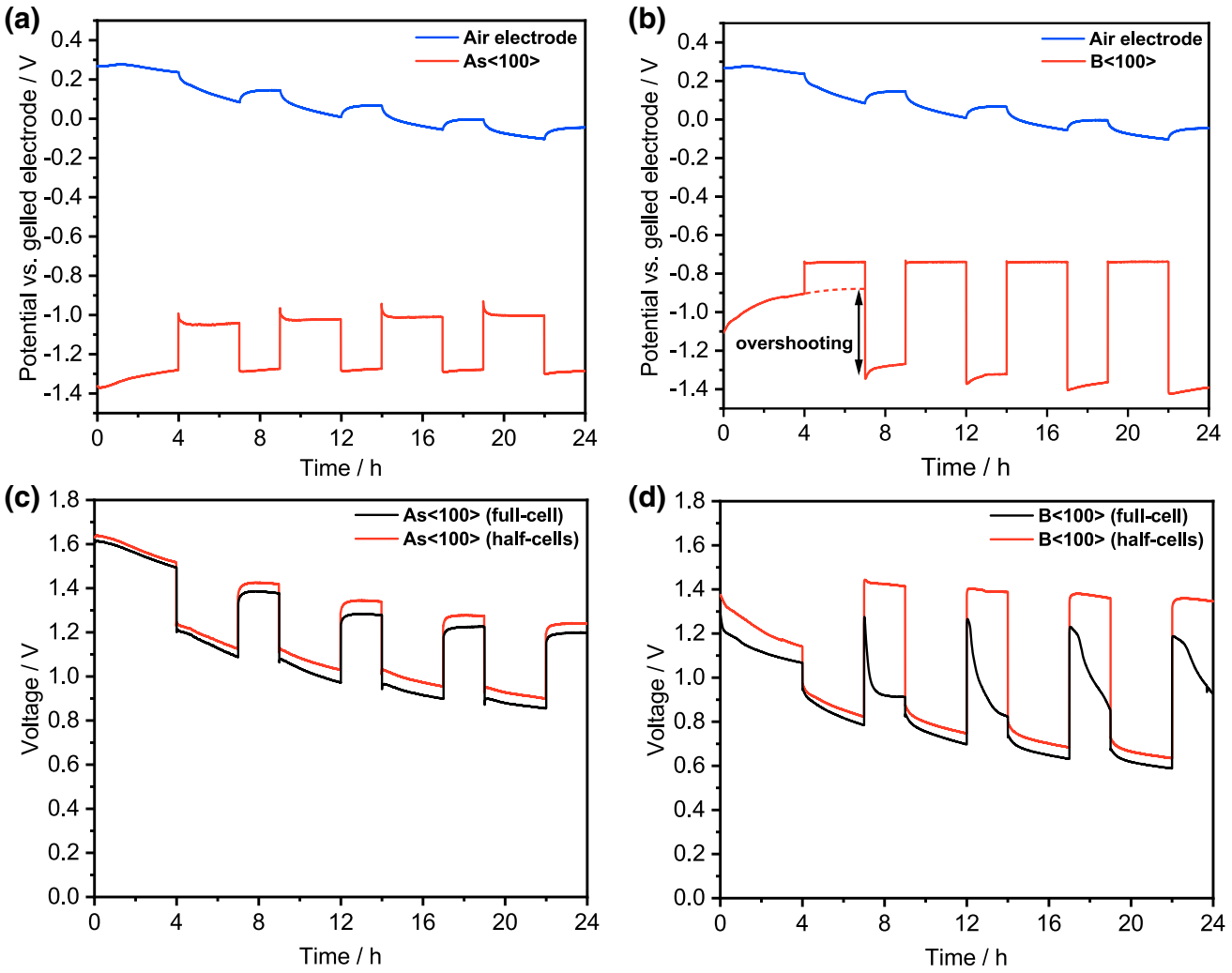

Fig. 4 Potential profiles during 24 h pulsed discharge experiments under 0.3 mA cm^{-2} for **a** half-cells with As-doped Si and carbon-based air cathode as working electrodes, **b** half-cells with B-doped Si and carbon-based air cathode as working electrodes with arrow indicating the amount of overshooting. **c** Comparison of the full-cell vs. half-cell discharge profiles for As-doped Si electrodes, **d** comparison of the full-cell vs. half-cell discharge profiles for B-doped Si electrodes

are different depending on presence or absence of air-electrodes in the setup. The findings are further confirmed by two experiments with full-cells in three electrode configuration that are assembled with a B-doped Si anode as working electrode and an air-electrode as counter electrode while measuring the potential of both electrodes versus the gel-based reference electrode. The potential profile of the air-electrode in the full-cell (Fig. 5a) is almost identical to the one obtained from the half-cell experiment (Fig. 4a). For the B-doped Si electrode in the full-cell, the discharge potential is stable at − 0.74 V which is the same as in the corresponding half-cell experiment. However, the OCP of the B-doped Si electrode after the discharge steps does not stabilize at − 1.3 V as in the half-cell level but relaxes back to − 0.85 V approximately after substantial overshooting to − 1.3 V. Very similar behavior of the potentials is also observed for a cell assembled in a three-electrode setup with a B-doped Si as working electrode, Pt counter electrode in which carbon powder retrieved from the air-electrode is added to the electrolyte (Fig. 5b).

The changes in potentials and the overshooting are, therefore, related to processes that modify in first instance the B-doped Si anodes. In the absence of carbon in the system during the discharge period, modifications of the B-doped Si-anode cause a permanent increase in the subsequent OCV (Fig. 5a). This modification might be due to the formation of a surface layer containing Si–F–B elements as shown in Fig. 5c (2nd state) [26]. In presence of carbon, the modifications are temporarily and seem to be counteracted by carbon (3rd to 4th state). The effects on OCV are fading with time and showing up in the form of overshooting effects. In both cases, the modifications

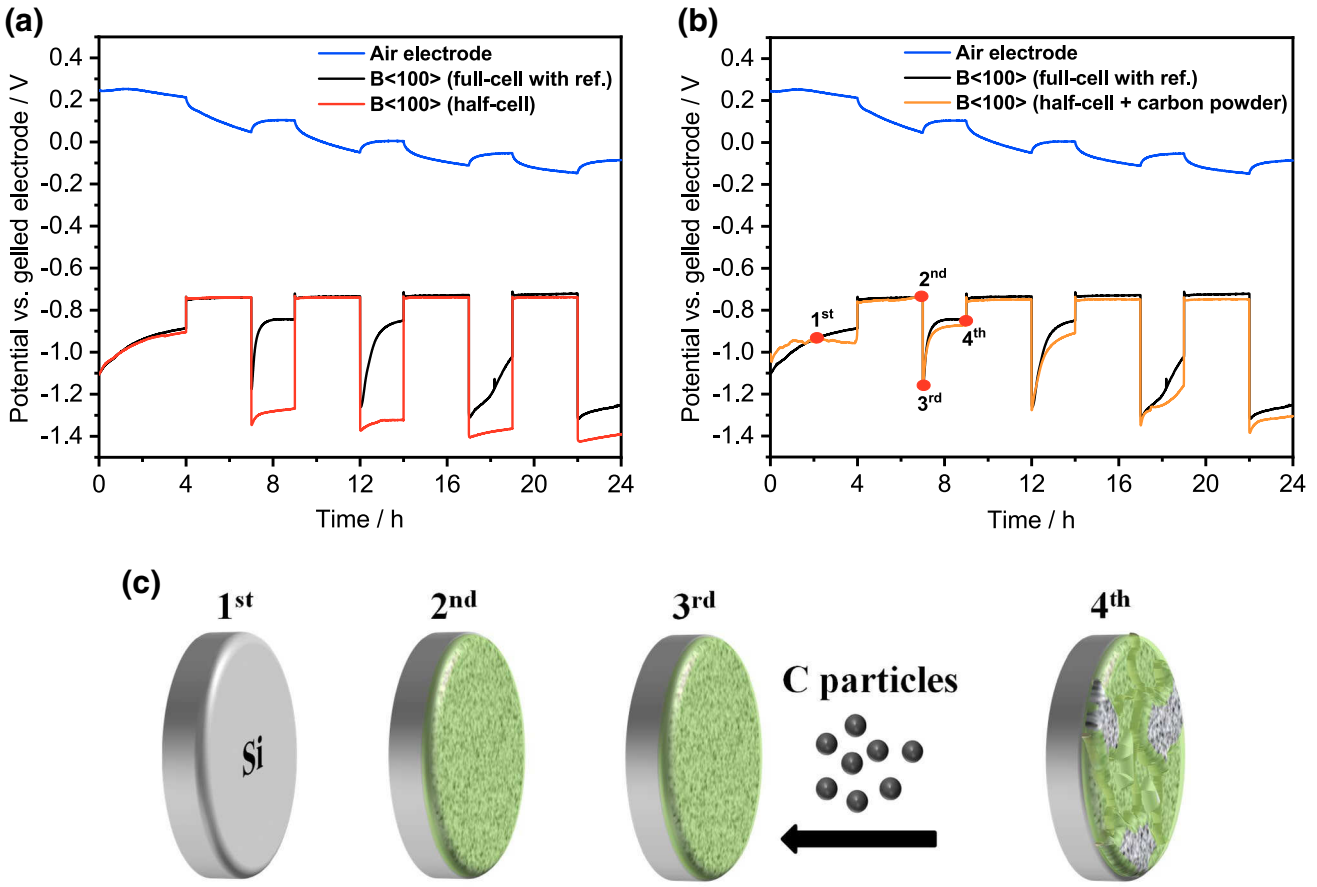

Fig. 5 Discharge profiles of Si–air cells with half-cell potentials of B-doped Si anodes and carbon-based air-electrodes during 24 h pulsed discharge with 0.3 mA cm^{-2}. **a** Half-cell vs. full-cell with three electrode configuration, **b** half-cell with carbon powder additive into electrolyte vs. full-cell with three electrode configuration, and **c** a proposed scheme of Si surfaces at different operation times as shown in **b**

affect only subsequent OCV, but not subsequent discharge potentials.

3.3 Corrosion

The corrosion rates for ⟨100⟩ As- and B-doped Si anodes under pulsed discharge at current densities of 0.1 and 0.3 mA cm^{-2} during 200 h operating time are depicted in Fig. 6. According to the corrosion analysis, the As-doped Si wafers readily corrode during the OCV periods while the B-doped Si wafers show almost no corrosion behavior; the corrosion rates under 200 h OCV are 3.1 nm min^{-1} for the former and 0.1 nm min^{-1} for the latter electrodes. Along with discharge, on the other hand, both types of electrodes reveal enhanced corrosion rates at longer pulses. Particularly for the higher current density, the increase is more pronounced. Under continuous discharge ($p = 1$), the corrosion rates for As-doped Si anodes amount to 4.6 nm min^{-1} and 7.9 nm min^{-1} at 0.1 mA cm^{-2} and 0.3 mA cm^{-2}, respectively. In case of B-doped Si anodes, the corrosion rates increase linearly with p for both current densities. The corrosion rates under continuous discharge are 2.2 nm min^{-1} at 0.1 mA cm^{-2} and 6.2 nm min^{-1} at 0.3 mA cm^{-2} current densities.

For the B-doped anodes, almost perfectly linear dependence of the corrosion rates on current pulse time fraction (p) suggests that the OCV corrosion rates and corrosion rates under discharge are weighed by the time under these regimes. The precondition for such behavior is that the corrosion rates are constant with time. In comparison to previous study [26] which reports corrosion rates for As- and B-doped Si wafers after 4 h OCV + 20 h discharge experiments (corresponding to $p = 0.83$) at various current densities, the corrosion rates of B-doped Si wafers within the current work match perfectly even though the total operation time is 200 h.

In contrast to that, compared to the reported OCV corrosion rates for As ⟨100⟩ Si anodes over 24 h [26], the

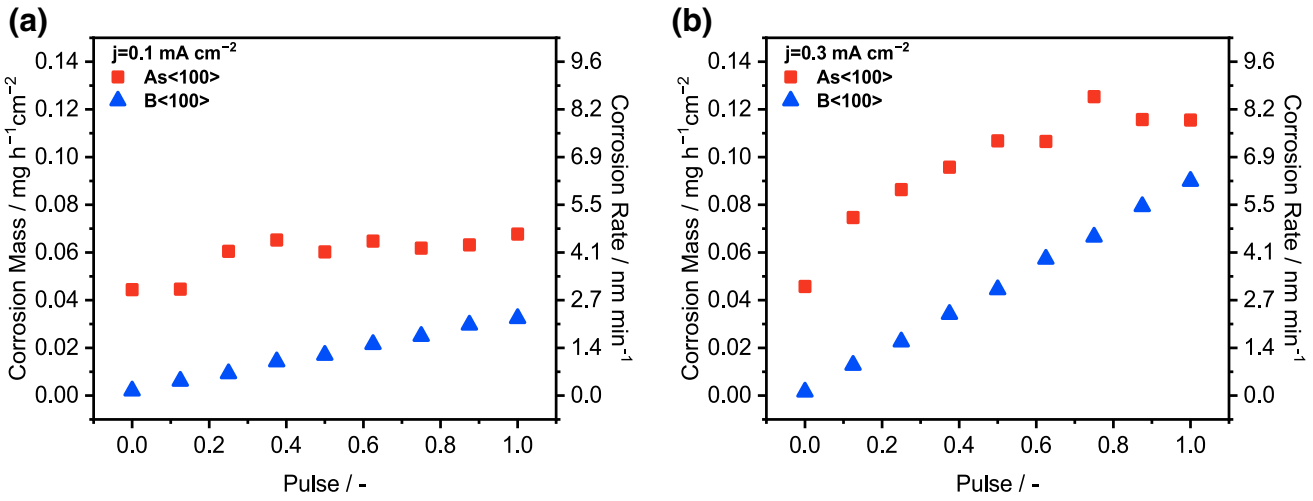

Fig. 6 Corrosion masses and corrosion rates for ⟨100⟩ oriented As- and B-doped Si anodes after 200 h pulsed operation **a** under a discharge current density of 0.1 mA cm^{-2} and **b** under a discharge current density of 0.3 mA cm^{-2}

corrosion rates during OCV increase significantly when the operating time is extended to 200 h; 1.6 nm min^{-1} for 24 h vs. 3.1 nm min^{-1} for 200 h. This relatively high corrosion rate during OCV is the reason for the enhanced corrosion rates observed for As-doped Si anodes for short pulses since the overall corrosion rate is mainly determined by the corrosion rate during OCV. At longer current pulses, however, the corrosion is strongly influenced by the corrosion rate during discharge because of short OCV durations. The resulting corrosion rates are only slightly increasing with p; because, the corrosion rate under current is almost constant with time as confirmed by the comparison to previous report [26].

According to the comparison of corrosion rates for B-doped and As-doped Si electrodes, the corrosion behavior of Si is clearly altered by the type of dopants and operation conditions. The lower corrosion rates are mainly achieved either by B-doping or low discharge current densities. At longer discharge durations (at higher p), especially for higher current densities, the corrosion rates are significantly enhanced for both dopants. This phenomenon somehow resembles the unusual feature of magnesium (or sometimes aluminium) in aqueous media known as the negative difference effect (NDE) [32–36]. According to this theory, in contrast to most metals, both the anodic reaction rate (oxidation of Mg) and cathodic reaction rate (hydrogen evolution)—hence the corrosion rate—are enhanced with an increase of the applied potential in the anodic direction. Consequently, there is a significant difference between the corrosion rates calculated with Faraday's law and the corrosion rates determined gravimetrically. Considering the previously reported corrosion rates of Si in both aqueous [17] and non-aqueous [26] media, a similar mechanism to NDE might also be possible for Si.

The corrosion (etch) rate reduction for highly doped Si electrodes has been widely investigated for semiconductor-related applications [30, 37–39]. The key factors, in this regard, are the concentration of dopants and the solutions by which Si is being etched. For example, the etch rate reduction of Si is mainly achieved in aqueous alkaline solutions [30, 39] while it is not observed in HF-based aqueous solutions [37, 38]. The critical doping concentration for B-doped Si (p-type) is around 2×10^{19} cm^{-3} whereas higher doping concentrations are needed for n-type Si at which the etch rate reduction occurs [39]. Until now, the mechanisms responsible for etch rate reduction of Si have not been understood well although several different models have been proposed [28]. In case of EMIm(HF)$_{2.3}$F electrolyte, the lower corrosion rates for B-doped Si electrodes (doping concentration $>2\times10^{19}$ cm^{-3}) evidence that etch rate reduction also takes place in this non-aqueous solution even though it is HF-based. This is confirmed by the potentiodynamic polarization experiments as B-doped Si electrodes resulting in lower corrosion rates and open-circuit potentials [13, 26]. Contrary to HF-based aqueous solutions, the etch rate reduction for B-doped electrodes in EMIm(HF)$_{2.3}$F could originate from the lack of water or from surface layers that consist of Si–F–B species. Further investigations are needed for better understanding of the behavior of Si in EMIm(HF)$_{2.3}$F.

3.4 Microstructure of anode surfaces after discharge

SEM images of the As- and B-doped Si anode surface morphologies after pulsed discharge with 0.3 mA cm^{-2} are shown in Fig. 7. There are marked differences between the As- and B-doped Si surfaces for all pulses. In particular for

the As-doped Si, even the pulse condition reveals quite pronounced effects on the surface morphologies.

Figure 7a illustrates a randomly textured rough surface full of hillocks for the As-doped Si anode after 200 h OCV (the analysis of the line and surface roughness parameters can be found in Fig. S1 and Table S1). Discharging the cell under $p = 0.125$ increases the roughness slightly; the area between the hillocks becomes larger (Fig. 7c). A pronounced difference on the surface morphologies appears for employing $p = 0.875$ pulse as shown in Fig. 7e. The surface is mostly covered with squared shallow pits while the border between them resembles pyramid-like structures. Along with the continuous discharge, the size of those shallow pits decreases while revealing the border structures more clearly (Fig. 7g).

Under the same cell operation conditions, B-doped Si anodes show much smoother surface morphologies even after the continuous discharge. Figure 7b depicts formation of few small pits while most of the surface remaining smooth after 200 h OCV. The surface becomes slightly rough when discharged under $p = 0.125$ (Fig. 7d). Under discharge with $p = 0.875$ and 1, the surface roughness is similar; however, few small dimples and many small pores appear along with longer current pulses (Fig. 7f, h).

Considering the nature of the electrolyte, one might expect isotropic etching behavior during OCV and formation of porous surface under anodic dissolution due to the single crystallinity of the silicon. The formation of a porous surface in conventional aqueous HF and non-aqueous $EMIm(HF)_{2.3}F$ solutions is mainly achieved under high-anodic current densities and/or potentials for both n- and p-type Si electrodes during relatively short operation times [28, 40–45]. Specifically for the $EMIm(HF)_{2.3}F$ solutions, different pore morphologies with widths ranging from 15 to 200 nm and depths up to 20 µm could be produced depending on the Si specifications and experimental conditions [43–45].

The $EMIm(HF)_{2.3}F$ electrolyte is a unique room temperature ionic liquid which provides high concentrations of fluoride anions. The fluoride anions, if exceeding a critical concentration, may react with the positively charged Si surface and initiate pit formation [45]. According to Raz et al., [45] the formation of porous surface on an n-type Si initiates once the anodic polarization starts. Polarizing Si anodically results in generation of Si–F bonds at the local spots which may cause a local increase in concentration of surface states on the Si surface. Surface states usually exist at small amount on Si surfaces at OCP and they are associated with the dissolution of silicon in acidic fluoride solutions [28]. Due to enhanced Si–F bonds at local spots, the dissolution of Si starts most likely in the form of pitting. The formed local pits initiate the porous surface formation and etching under anodic potentials. In the present study, due to the relatively low applied current densities (in comparison to previous studies [43, 45]), the surface of As-doped Si electrodes only possesses the squared pit formation in a microscale without any visible porous structures under SEM—formation of such large squared pits on Si electrodes are being reported for the first time in $EMIm(HF)_{2.3}F$ solutions. There could still be some nano-pores formed as shown in [26], or as shown for B-doped Si surfaces (Fig. 7), however, at much smaller dimensions comparing to the previous studies [43–45].

3.5 Experimental results on specific energies

Based on the results on mean voltages during discharge E_{dis}, discharge currents I_{dis} and times t_{dis}, and mass changes Δm_{tot}, the specific energies w_s delivered by the Si–air cells under pulsed operation can be calculated according to

$$w_s = (E_{dis} \cdot I_{dis} \cdot t_{dis})/\Delta m_{tot}. \quad (4)$$

The specific energies depending on the current pulse time fraction for cells with As- and B-doped Si anodes are illustrated in Fig. 8. Regardless of the applied current density, B-doped Si electrodes provide remarkably higher specific energies at low-current pulse time fractions. For example, at $p = 0.125$, specific energies of 860 and 950 Wh kg_{Si}^{-1} are realized under 0.1 and 0.3 mA cm^{-2}, respectively; while cells with As-doped Si anodes result in 250 and 350 Wh kg_{Si}^{-1}. At high-current pulse time fractions, however, both Si types reveal almost the same discharge-specific energies for 0.1 mA cm^{-2} whereas application of higher current density leveled the values for As-doped Si electrodes even at relatively lower current pulse time fractions.

During the OCV periods, anode material is oxidized without delivering electrical energy owing to corrosion reactions. Thereby, on the one hand the specific energies tend to become lower with decreasing current pulse time fractions (longer OCV); on the other hand the higher discharge voltages along with short current pulse time favor an increase of specific energies. Quantitatively the impact on specific energies depends on the extent of OCV corrosion rates and therefore is quite different for As- and B-doped Si anodes. For the As-doped Si, the OCV corrosion rates are around 65 and 40% of the corrosion present under continuous discharge at 0.1 and 0.3 mA cm^{-2}, respectively. Consequently, there is a marked reduction in specific energies when operating the cells in pulsed mode, e.g. 350 Wh kg_{Si}^{-1} with $p = 0.125$ vs. 950 Wh kg_{Si}^{-1} with $p = 1$ under 0.3 mA cm^{-2}. In contrast to that, negligible OCV corrosion in the cells with B-doped Si anodes results in quite similar-specific energies for most of the pulse fractions with a slight tendency towards enhanced specific energies at shorter current pulse time fractions.

In general, the shift in the ranking of the anode materials is mainly originating from the differences in the OCV

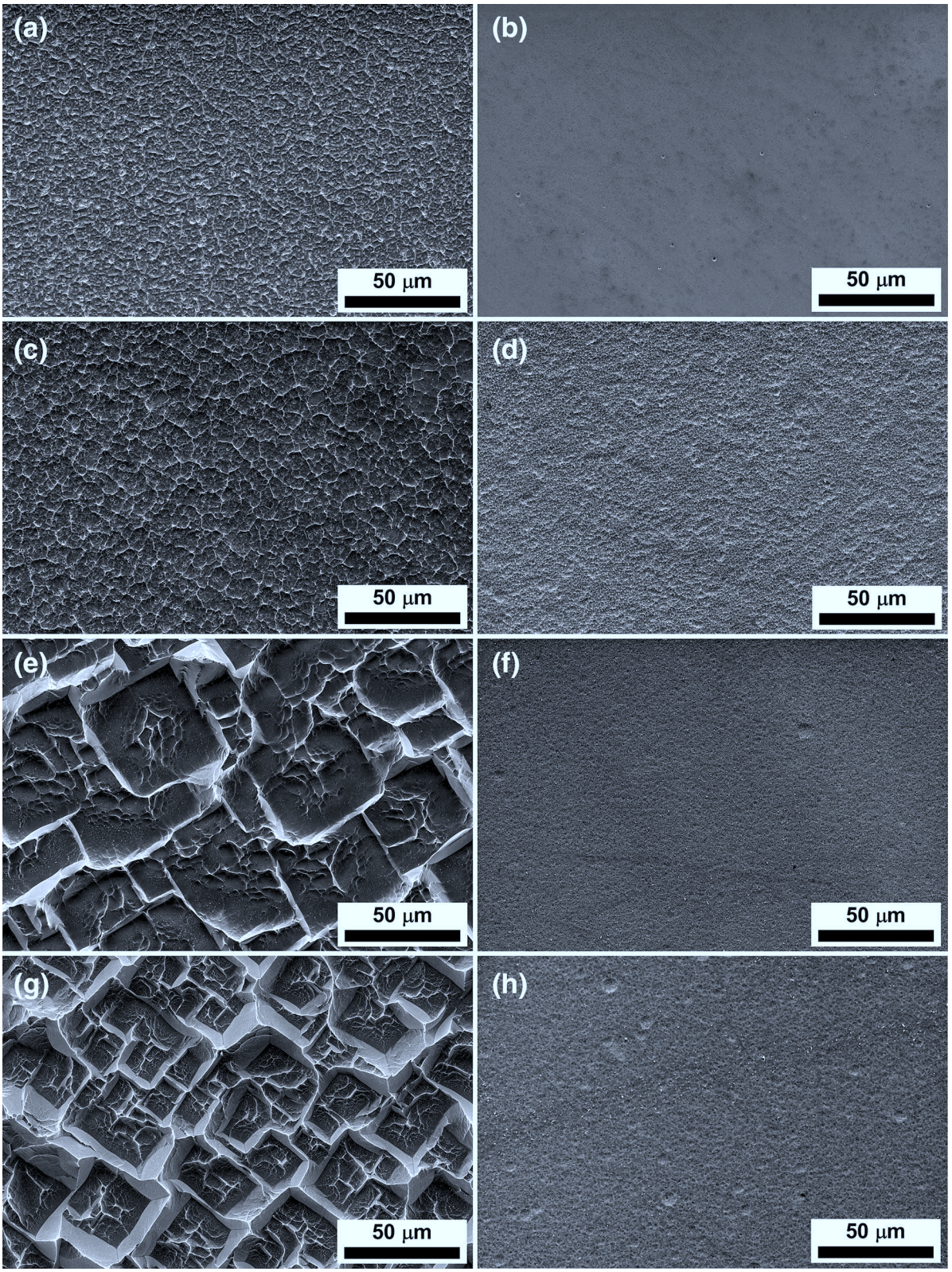

Fig. 7 Surface images of the Si anodes after 200 h pulsed discharge with 0.3 mA cm^{-2}. **a** As-doped Si with $p=0$, **b** B-doped Si with $p=0$, **c** As-doped Si with $p=0.125$, **d** B-doped Si with $p=0.125$, **e** As-doped Si with $p=0.875$, **f** B-doped Si with $p=0.875$, **g** As-doped Si with $p=1$, and **h** B-doped Si with $p=1$

corrosion rates. Operating the cells at moderately low-current pulse time fractions decreases the specific energies for the As-doped Si anodes substantially; whereas those for the B-doped Si anodes are slightly dependent on p. Along with continuous discharge, however, the differences in the discharge voltages compensate the OCV corrosion effect in favor of the As ⟨100⟩ Si anodes especially under higher current density.

3.6 Approach for calculation of specific energies under pulsed discharge

Considerable efforts are required to provide a compound view on cell performance under pulsed discharge operating conditions based on merely experimental work. Therefore, an approach to establish the most essential information on specific energies by combining a reduced number of experiments with calculations is addressed.

Point of departure is the formulation of specific energies

$$w_s(p) = (E_{dis}(p) \cdot I_{dis} \cdot t_{dis}(p))/\Delta m_{tot}(p). \quad (5)$$

In the experimental approach E_{dis} and Δm_{tot} have to be measured in individual experiments for each current pulse time fraction. Assuming that (i) the mean discharge voltages under current pulses E_{dis} can be approximated by the mean voltages under continuous discharge E^* (ii) the corrosion under pulsed discharge is a linear combination of the corrosion under OCV and under continuous discharge weighed by the time in the respective states, and (iii) the corrosion rates are constant with time; the expression for the specific energy can be reformulated to

$$w_s(p) = (E^* \cdot I_{dis} \cdot t_{dis}(p))/(\Delta m_{dis}(p) + c_{dis} \cdot t_{dis}(p) + c_{ocv} \cdot t_{ocv}(p)), \quad (6)$$

where c_{dis} and c_{ocv} are the corrosion rates under continuous discharge and OCV while Δm_{dis} is the amount of active mass required to generate desired electrical energy. For a given specification of the pulsed discharge experiment I_{dis}, t_{dis}, t_{ocv} and Δm_{dis} are defined by the experimental setup. According to assumption (i) and (ii), E^* is evaluated from the continuous discharge profile, while the corrosion rates c_{ocv} and c_{dis} can be determined from an OCV and a continuous discharge experiment. Thus, an estimation of the specific energies depending on current pulse time fraction based on only two experiments—the OCV and the continuous discharge runs—can be provided.

The results of the calculations for the specific energies for the cells with As-doped Si and B-doped Si anodes are depicted and compared to the experimental data in Fig. 9a, b. The specific energies calculated for the As-doped Si anodes match the data determined in the experiments quite well. Good agreement between experimental and calculated specific energies is also obtained for the pulsed discharge of the cells with B-doped Si anodes under current densities of 0.1 mA cm^{-2}. However, under operation at 0.3 mA cm^{-2} the calculations underestimate the specific energies for these types of cells by approximately 15% in the range of low to medium current pulse time fractions. In terms of specific capacities (Fig. 9c, d) and anode mass conversion efficiencies (Fig. 9e, f), the calculated data for B-doped Si cells show a good agreement with the experimental data while there is approximately 10% difference in the comparison of the As-doped Si data for 0.3 mA cm^{-2} discharge pulses. The anode mass conversion efficiencies (utilization efficiencies),

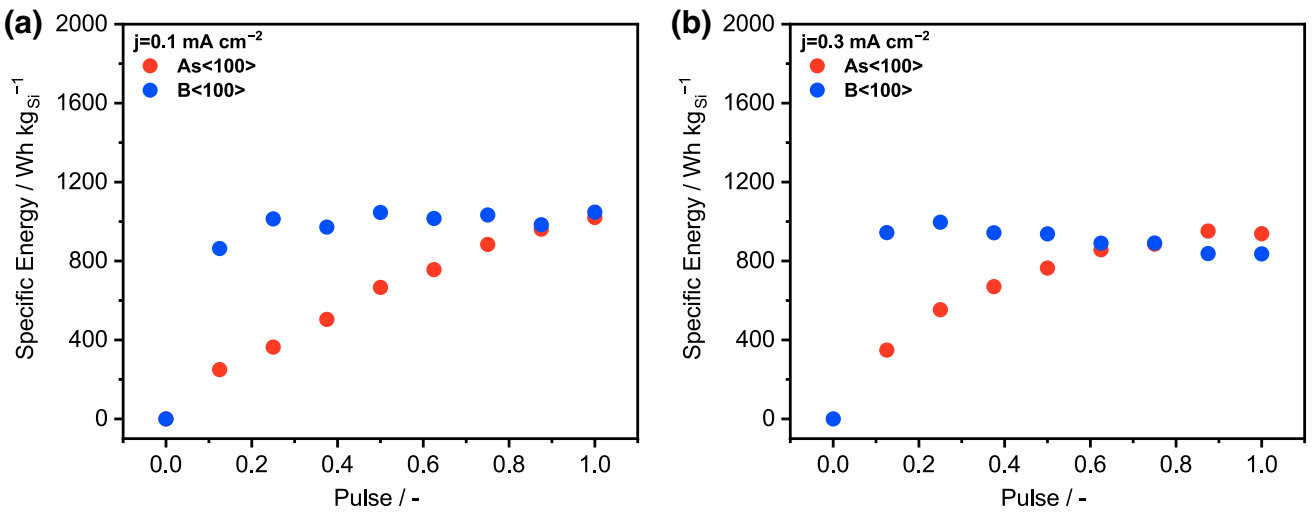

Fig. 8 Influence of the current pulse time fractions on the discharge-specific energies of Si–air cells with As- and B-doped Si anodes after 200 h cell operation with **a** discharge current density of 0.1 mA cm^{-2} and **b** discharge current density of 0.3 mA cm^{-2}

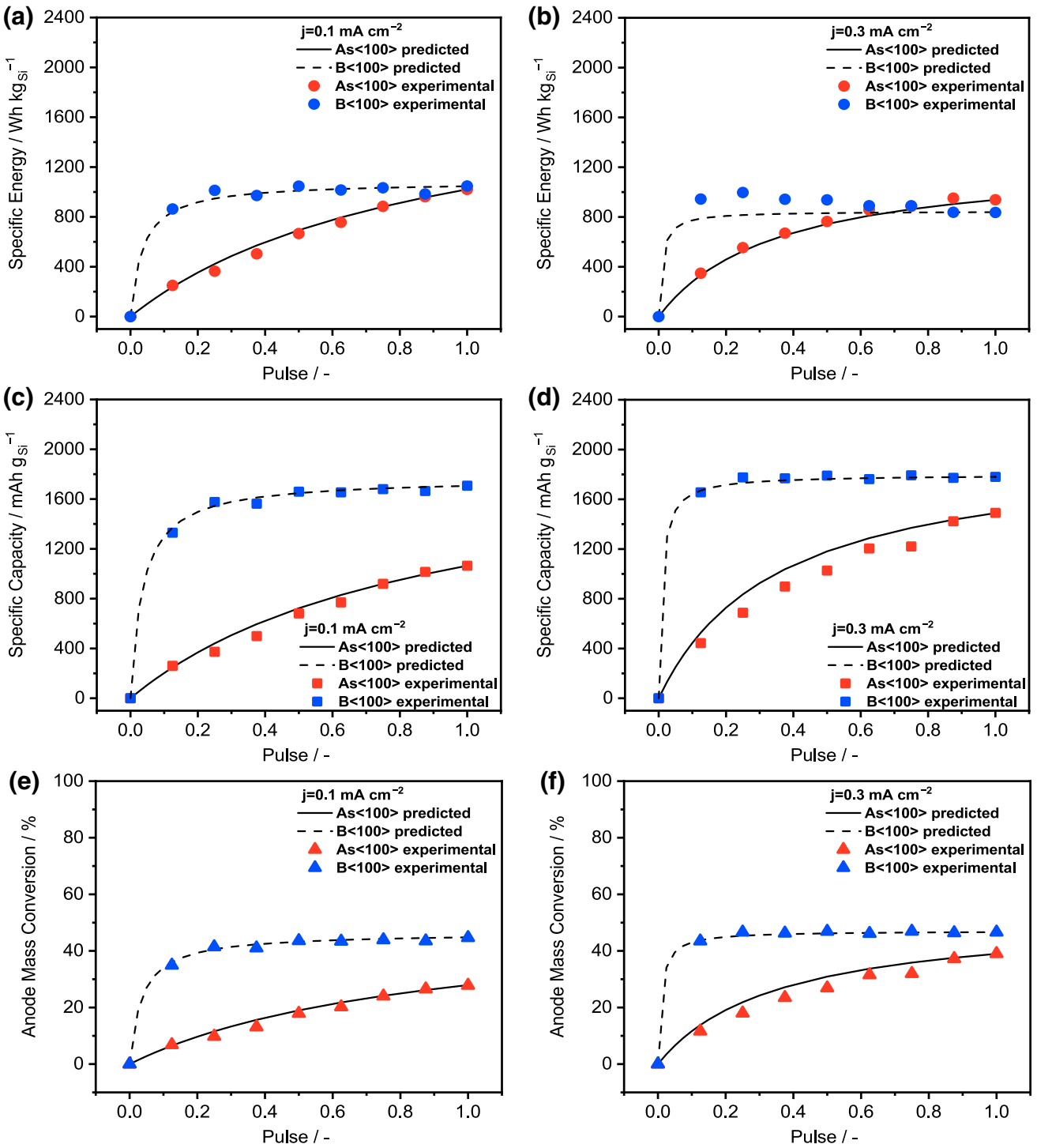

Fig. 9 Experimental vs. calculated values of Si–air cells depending on current pulse time fraction for **a** specific energies for 0.1 mA cm^{-2}, **b** specific energies for 0.3 mA cm^{-2}, **c** specific capacities for 0.1 mA cm^{-2}, **d** specific capacities for 0.3 mA cm^{-2}, **e** anode mass conversion efficiencies for 0.1 mA cm^{-2}, and **f** anode mass conversion efficiencies for 0.3 mA cm^{-2}

within this context, correspond to the ratio between the mass loss due to electrochemical discharge reaction and the total mass loss of the Si electrodes. It can be clearly seen from Fig. 9e, f that, B-doped Si electrodes with up to 46% surpass the As-doped Si electrodes in terms of anode mass conversion efficiencies under any pulse conditions. Originating from the same reason—lower corrosion rates—the specific capacities as high as 1790 mAh g_{Si}^{-1} obtained

from the cells provide the same trend in favor of B-doped Si electrodes.

The analysis of the specific capacities and anode mass conversion efficiencies demonstrate that the discharge conditions affect the performance of cells with B-doped Si only slightly—especially at higher current densities—whereas cells with As-doped Si are highly dependent on the mode of operation. Hence, employing Si electrodes with B-dopant provides robust batteries which are also flexible in terms of operating conditions. However, in comparison to theoretical specific capacity of Si, 3820 mAh g_{Si}^{-1}, the practical specific capacities (up to 1790 mAh g_{Si}^{-1}) and mass conversion efficiencies (up to 46%) indicate that there is still room for further improvement. Nonetheless, among other resource-efficient metal–air batteries, 1790 mAh g_{Si}^{-1} is one of the highest specific capacities that is reported practically.

Considering the comparatively simple approach for the calculations, the overall matching of the experimental data is good; however, limitations of the method become apparent when comparing the calculated vs. the experimental results for the specific capacities (Fig. 9c, d). For the cells with the B-doped Si anodes under 0.3 mA cm^{-2} pulsed discharge, the experimental vs. the calculated specific capacities c_s are quite close, whereas the specific energies w_s are underestimated by the latter. The relation $w_s = E \cdot Q_s$ implies, that the approximation of E_{dis} (mean voltage under current pulse) by E^* (mean voltage under continuous discharge) has to be reconsidered. Moreover, differences in experimental vs. calculated specific capacities for the cells with As-doped Si anodes under 0.3 mA cm^{-2} can be attributed to the OCV corrosion rates being non-constant over time.

Overall, there are indeed limitations existing for this simple approach used in the calculations which might be improved by further modifications. Nonetheless, the present approach provides the cell discharge parameters such as specific energy, specific capacity, and anode mass conversion efficiency under pulsed operation conditions with at least 85% accuracy while requiring minimum experimental effort. Furthermore, this method can also be applied to other similar type of metal–air batteries (e.g. zinc, iron, aluminium, etc.) as long as the assumptions are approximately met.

4 Conclusions

The discharge performance of Si–air cells with ⟨100⟩ oriented As- and B-doped Si anodes under dynamic conditions were studied basing on pulsed discharge experiments. Both anode types could be discharged with 0.1 and 0.3 mA cm^{-2} over 200 h under current pulse time fractions varying from $p = 0.125$ to 1. In general, As-doped Si anodes provide higher OCV and discharge voltages than B-doped Si anodes. The latter reveal overshooting behavior during the OCV periods following each discharge pulse steps. In half-cell experiments, it was proposed that each discharge step activates surface processes that lead to higher OCPs in the following periods while the effects of activation do not influence the subsequent discharge potentials. The stability of the activated surface processes are highly dependent on the presence of carbon-based air electrode. Under OCV conditions, B-doped Si anodes showed negligible corrosion rates which were increased almost linearly with current pulse time fractions. The lower corrosion rates observed for B-doped Si are possibly caused by etch rate reduction originating from high doping concentrations. As-doped Si anodes, on the other hand, readily corrode under OCV and the rates depend on the total OCV duration. For both cells, imposing anodic discharge currents enhances the corrosion rates depending on the current levels. Although differences on the surface microstructures influenced by the current pulse time fraction were observed for As-doped Si, there was no significant effect on the electrochemistry. Evaluation of the discharge-specific energies revealed that at low to medium current pulse fractions B-doped Si anodes provided higher values (up to 1000 Wh kg_{Si}^{-1} at $p = 0.25$); in case of As-doped Si anodes, continuous discharge or medium to high-current pulse fractions are necessary to reach or slightly surpass the specific energies of B-doped Si. Concerning the specific capacities (up to 1790 mAh g_{Si}^{-1}) and the anode mass conversion efficiencies (up to 46%), B-doped Si anodes surpass As-doped Si for each current pulse fraction. A general approach was proposed to calculate the most essential battery parameters—specific energy, specific capacity, and anode mass conversion efficiency—by basing on only two experimental values obtained from continuous OCV and discharge profiles. The experimental results for pulsed discharge battery operations could be predicted with at least 85% accuracy.

Overall, both As- and B-doped Si anodes provide advantages depending on the requirements of specific applications. For a dynamic mode of operation, where cells are discharged at moderate currents from time to time with different durations or they are kept at storage for relatively long times, B-doped Si electrodes should be the choice of anode material for non-aqueous Si–air cells. Nonetheless, more investigations are required on the corrosion inhibition in order to improve the discharge performance and shelf-life of Si–air cells.

Acknowledgements This work was supported by the German Federal Ministry of Education and Research (BMBF) within the Project MeLuBatt (03XP0110F), by the 2nd Israel National Research Center for Electrochemical Propulsion (INREP 2), and by the Grand Technion Energy Program (GTEP).

References

1. Li Y, Lu J (2017) Metal–air batteries: will they be the future electrochemical energy storage device of choice? ACS Energy Lett 2:1370–1377. https://doi.org/10.1021/acsenergylett.7b00119
2. Lee J-S, Tai Kim S, Cao R et al (2011) Metal-air batteries with high energy density: Li-air versus Zn-air. Adv Energy Mater 1:34–50. https://doi.org/10.1002/aenm.201000010
3. Rahman MA, Wang X, Wen C (2013) High Energy density metal-air batteries: a review. J Electrochem Soc 160:A1759–A1771. https://doi.org/10.1149/2.062310jes
4. Gelman D, Shvartsev B, Ein-Eli Y (2016) Challenges and prospect of non-aqueous non-alkali (NANA) metal-air batteries. Top Curr Chem 374:82. https://doi.org/10.1007/s41061-016-0080-9
5. McKerracher RD, Ponce de Leon C, Wills RGA et al (2015) A review of the iron-air secondary battery for energy storage. ChemPlusChem 80:323–335. https://doi.org/10.1002/cplu.201402238
6. Weinrich H, Gehring M, Tempel H et al (2018) Impact of the charging conditions on the discharge performance of rechargeable iron-anodes for alkaline iron–air batteries. J Appl Electrochem 48:451–462. https://doi.org/10.1007/s10800-018-1176-4
7. Elia GA, Marquardt K, Hoeppner K et al (2016) An overview and future perspectives of aluminum batteries. Adv Mater 28:7564–7579. https://doi.org/10.1002/adma.201601357
8. Ryu J, Park M, Cho J (2018) Advanced technologies for high-energy aluminum-air batteries. Adv Mater. https://doi.org/10.1002/adma.201804784
9. Weinrich H, Durmus YE, Tempel H et al (2019) Silicon and iron as resource-efficient anode materials for ambient-temperature metal-air batteries: a review. Materials (Basel) 12:2134. https://doi.org/10.3390/ma12132134
10. Vesborg PCK, Jaramillo TF (2012) Addressing the terawatt challenge: scalability in the supply of chemical elements for renewable energy. RSC Adv 2:7933. https://doi.org/10.1039/c2ra20839c
11. U.S. Geological Survey (2017) Mineral commodity summaries 2017
12. Kalz KF, Kraehnert R, Dvoyashkin M et al (2017) Future challenges in heterogeneous catalysis: understanding catalysts under dynamic reaction conditions. ChemCatChem 9:17–29. https://doi.org/10.1002/cctc.201600996
13. Cohn G, Ein-Eli Y (2010) Study and development of non-aqueous silicon-air battery. J Power Sources 195:4963–4970. https://doi.org/10.1016/j.jpowsour.2010.02.070
14. Durmus YE, Aslanbas Ö, Kayser S et al (2017) Long run discharge, performance and efficiency of primary silicon–air cells with alkaline electrolyte. Electrochim Acta 225:215–224. https://doi.org/10.1016/j.electacta.2016.12.120
15. Zhong X, Zhang H, Liu Y et al (2012) High-capacity silicon-air battery in alkaline solution. Chemsuschem 5:177–180. https://doi.org/10.1002/cssc.201100426
16. Park DW, Kim S, Ocon JD et al (2015) Controlled electrochemical etching of nanoporous Si anodes and its discharge behavior in alkaline Si–air batteries. ACS Appl Mater Interfaces 7:3126–3132. https://doi.org/10.1021/am507360e
17. Durmus YE, Montiel Guerrero SS, Aslanbas Ö et al (2018) Investigation of the corrosion behavior of highly As-doped crystalline Si in alkaline Si–air batteries. Electrochim Acta 265:292–302. https://doi.org/10.1016/j.electacta.2018.01.145
18. Hagiwara R, Hirashige T, Tsuda T, Ito Y (2002) A highly conductive room temperature molten fluoride: EMIF·2.3HF. J Electrochem Soc 149:D1–D6. https://doi.org/10.1149/1.1421606
19. Matsumoto K, Hagiwara R, Yoshida R et al (2004) Syntheses, structures and properties of 1-ethyl-3-methyl-imidazolium salts of fluorocomplex anions†. Dalton Trans. https://doi.org/10.1039/B310162B
20. Hagiwara R, Nakamori Y, Matsumoto K, Ito Y (2005) The effect of the anion fraction on the physicochemical properties of EMIm(HF)nF (n = 1.0–2.6). J Phys Chem B 109:5445–5449. https://doi.org/10.1021/jp047006l
21. Shvartsev B, Gelman D, Starosvetsky D, Ein-Eli Y (2016) Silicon oxide dissolution in fluorohydrogenates ionic liquid. J Electrochem Soc 163:E135–E141. https://doi.org/10.1149/2.0971605jes
22. Gelman D, Shvartsev B, Wallwater I et al (2017) An aluminum–ionic liquid interface sustaining a durable Al-air battery. J Power Sources 364:110–120. https://doi.org/10.1016/j.jpowsour.2017.08.014
23. Cohn G, Starosvetsky D, Hagiwara R et al (2009) Silicon–air batteries. Electrochem Commun 11:1916–1918. https://doi.org/10.1016/j.elecom.2009.08.015
24. Cohn G, Eichel R-A, Ein-Eli Y (2013) New insight into the discharge mechanism of silicon-air batteries using electrochemical impedance spectroscopy. Phys Chem Chem Phys 15:3256–3263. https://doi.org/10.1039/c2cp43870d
25. Jakes P, Cohn G, Ein-Eli Y et al (2012) Limitation of discharge capacity and mechanisms of air-electrode deactivation in silicon-air batteries. Chemsuschem 5:2278–2285. https://doi.org/10.1002/cssc.201200199
26. Durmus YE, Jakobi S, Beuse T et al (2017) Influence of dopant type and orientation of silicon anodes on performance, efficiency and corrosion of silicon–air cells with $EMIm(HF)_{2.3}F$ electrolyte. J Electrochem Soc 164:A2310–A2320. https://doi.org/10.1149/2.0301712jes
27. Shvartsev B, Cohn G, Shasha H et al (2013) Reference electrode assembly and its use in the study of fluorohydrogenate ionic liquid silicon electrochemistry. Phys Chem Chem Phys 15:17837–17845. https://doi.org/10.1039/c3cp52661e
28. Zhang XG (2001) Electrochemistry of silicon and its oxide. Springer, New York
29. Memming R (2015) Semiconductor electrochemistry, 2nd edn. Wiley-VCH Verlag GmbH and Co, KGaA, Weinheim
30. Palik ED, Bermudez VM, Glembocki OJ (1985) Ellipsometric study of the etch-stop mechanism in heavily doped silicon. J Electrochem Soc 132:135–141. https://doi.org/10.1149/1.2113747
31. Chen L-C (1995) The band model and the etching mechanism of silicon in aqueous KOH. J Electrochem Soc 142:170. https://doi.org/10.1149/1.2043860
32. Song GL, Atrens A (1999) Corrosion mechanisms of magnesium alloys. Adv Eng Mater 1:11–33. https://doi.org/10.1002/(SICI)1527-2648(199909)1:1%3c11:AID-ADEM11%3e3.0.CO;2-N
33. Bender S, Goellner J, Heyn A, Schmigalla S (2012) A new theory for the negative difference effect in magnesium corrosion. Mater Corros 63:707–712. https://doi.org/10.1002/maco.201106225
34. Dražić DM, Popić JP, (1999) Corrosion rates and negative difference effects for Al and some Al alloys. J Appl Electrochem 29:43–50. https://doi.org/10.1023/A:1003447018115
35. Smoljko I, Gudić S, Kuzmanić N, Kliskić M (2012) Electrochemical properties of aluminium anodes for Al/air batteries with aqueous sodium chloride electrolyte. J Appl Electrochem 42:969–977. https://doi.org/10.1007/s10800-012-0465-6
36. Frankel GS, Fajardo S, Lynch BM (2015) Introductory lecture on corrosion chemistry: a focus on anodic hydrogen evolution on

Al and Mg. Faraday Discuss 180:11–33. https://doi.org/10.1039/C5FD00066A
37. Petersen KE (1982) Silicon as a mechanical material. Proc IEEE 70:420–457. https://doi.org/10.1109/PROC.1982.12331
38. Zhang XG (1989) Porous silicon formation and electropolishing of silicon by anodic polarization in HF solution. J Electrochem Soc 136:1561. https://doi.org/10.1149/1.2096961
39. Seidel H, Csepregi L, Heuberger A, Baumgartel H (1990) Anisotropic etching of crystalline silicon in alkaline solutions 2. J Electrochem Soc 137:3626–3632. https://doi.org/10.1149/1.2086278
40. Lehmann V (1990) Formation mechanism and properties of electrochemically etched trenches in n-type silicon. J Electrochem Soc 137:653. https://doi.org/10.1149/1.2086525
41. Smith RL, Collins SD (1992) Porous silicon formation mechanisms. J Appl Phys. https://doi.org/10.1063/1.350839
42. Lehmann V, Stengl R, Luigart A (2000) On the morphology and the electrochemical formation mechanism of mesoporous silicon. Mater Sci Eng B 69:11–22. https://doi.org/10.1016/S0921-5107(99)00286-X
43. Raz O, Starosvetsky D, Tsuda T et al (2007) Macroporous silicon formation on n-Si in room-temperature fluorohydrogenate ionic liquid. Electrochem Solid State Lett 10:D25–D28. https://doi.org/10.1149/1.2409058
44. Tsuda T, Nohira T, Amezawa K et al (2008) Anodic electrode reaction of p-type silicon in 1-ethyl-3-methylimidazolium fluorohydrogenate room-temperature ionic liquid. Electrochim Acta 53:3650–3655. https://doi.org/10.1016/j.electacta.2007.12.027
45. Raz O, Shmueli Z, Hagiwara R, Ein-Eli Y (2010) Porous silicon formation in fluorohydrogenate ionic liquids. J Electrochem Soc 157:H281–H286. https://doi.org/10.1149/1.3273082